Image-based computational modeling of blood flow in a porcine aorta bypass graft

By V. Favier AND C. A. Taylor †

1. Motivation and objectives

Even though pathological factors are known to characterize the development of vascular diseases, mechanical factors play a major role in their localization and progression. For example, fluid mechanic factors contribute to the initiation of atherosclerosis: plaque formation is more likely to occur in recirculation areas, downstream of arterial bifurcations and bends. It has been observed that, beside mediating the generation of diseases, local hemodynamic parameters enhance their growth. In complex flow areas, low wall shear stresses and high residence time are thought to exacerbate the chemical processes of wall thickening and clotting (cell proliferation in the inner layer of the vessels, surface damage of the endothelium cell layer at the interface of blood and the vessels, Dilley, Mc Geachie & Prendergast 1988; Gewertz *et al.* 1992).

Understanding these phenomena is important not only in research on diseases but also in surgery planning and in the development of artificial devices. Obstruction and failure of a bypass-graft operation may occur if the chemical reactions for thrombosis are activated at the wound where the bypass is added, and can further be maintained because of the sensitivity of the human cardiovascular system to a foreign body and favorable local hemodynamics, like flow stasis.

Numerous studies, both experimental and numerical, have focused on assessing these hypotheses and characterizing the level of importance of fluid quantities in the past few years. Nevertheless, how fluid mechanics and diseases interact remains unclear due to the variety of parameters required to describe the full physics of blood flow.

Non-invasive magnetic resonance imaging (MRI) and ultrasound techniques have been applied to *in vitro* studies on simple geometries (pipes, branches,...) and have shown their ability to measure accurate velocities and characterize flow patterns (Botnar *et al.* 2000). Significant progress in those imaging tools now make it possible to visualize large areas of the cardiovascular tree, observe moving vessel walls and measure velocities *in vivo*.

Numerical simulation is a very attractive tool to access fluid parameters that are difficult to obtain experimentally (full velocity fields, shear stresses,...). Moreover, numerical techniques enable the investigation of the effect of geometric and flow-rate modifications in the studied model. Computations of blood flow in idealized models of the cardiovascular system have been extensively studied. Perktold and colleagues examined blood flow in rigid and deformable models of carotid arteries (Perktold, Resch & Peter 1991; Perktold & Rappitsch 1995). Taylor *et al.* quantified blood flow in an idealized model of the human abdominal aorta under resting and exercise conditions (Taylor, Hughes & Zarins 1998a; Taylor, Hughes & Zarins 1999). Others examined blood flow in models of the end-to-side anastomosis (downstream connection of the end of a bypass graft to side of a host artery, Milner *et al.* 1998; Taylor, Hughes & Zarins 1998b).

† Stanford University, Mechanical Engineering & Surgery

Velocity profile comparisons between *in vitro* experiments and computation of blood flow using the same geometry have been successful in idealized models and also more complex cases. Taylor, Hughes & Zarins (1996), Milner *et al.* (1998), Cebral & Lohner (2001) have extracted realistic models of vessels from volumetric MRI or computed tomography (CT) in order to reproduce the complex anatomy of a patient.

Nevertheless, the combination of medical imaging techniques to extract geometric models and numerical simulation in *in vitro* cases only enables one to study pulsatile blood flow with significant assumptions about inflow boundary conditions. Measuring physiological flow waveforms *in vivo* and using them as data input to the experiment or the simulation does not insure that the velocity profile is realistic.

Ku *et al.* 2002 used a Dacron band to create a restriction (stenosis) in the descending thoracic aorta of pigs and then bypassed this stenosis with a Dacron graft. This aorto-aorto bypass graft was imaged using magnetic resonance angiography (MRA) and blood-flow velocity was measured in the aorta above the proximal connection of the graft to the aorta, using phase-contrast magnetic resonance imaging (PC-MRI). This flow velocity data was used to calculate the volumetric flow rate which in turn was used to prescribe fully-developed pulsatile flow boundary conditions (based on Womersley theory) at the inlet of the computational model. Computed flow rates in the bypass graft and native aorta compared favorably to the flow rates obtained from PC-MRI measurements in these locations. A limitation of this prior investigation is that a Womersley boundary condition was employed, and the effect of this idealized boundary condition on blood-flow rate and velocity patterns was not examined.

In this paper, we describe the effect of inflow boundary conditions on flow rate and velocity in the porcine aorto-aorto bypass model. We compare results of computational solutions performed using a Womersley inflow boundary condition and inflow velocity mapped directly from the PC-MRI data (*in vivo* experiments by Ku *et al.* 2002).

2. Methods

The anatomic model is constructed from MRA data as follows. A vessel path is identified and two-dimensional slice planes are positioned along this path in the volumetric image data. A level-set method is used to extract closed curves representing the vessel boundary in each two-dimensional plane (Wang *et al.* 1999). A surface is lofted through these curves and a solid model constructed. (see figure 1).

An automatic finite-element mesh generator is used to discretize the solid model (SCOREC, Rensselaer Polytechnic Institute). For the calculations described herein, a 1.2 million tetrahedral element mesh was used (figure 1).

As a first approximation we assume that the vessel walls are rigid and that blood behaves as a Newtonian fluid (Taylor *et al.* 1999). With these simplifications, the incompressible Navier-Stokes equations describe the problem.

$$\begin{aligned} u_{i,i} &= 0 \\ \dot{u_i} + u_j u_{i,j} &= -(p_{,i}/\rho) + \tau_{ij,j} + f_i \end{aligned} \tag{2.1}$$

The density ρ is constant, u_i is the i^{th} component of the velocity, p the pressure, f_i the prescribed body force, and τ_{ij} the viscous stress tensor given by $\tau_{ij} = \nu(u_{i,j} + u_{j,i})$, $\nu = \mu/\rho$ is the kinematic viscosity.

Velocity and pressure are solved using a stabilized finite-element method (Taylor *et al.* 1998, Jansen *et al.* 2000). A traction-free boundary condition is used at the outlet.

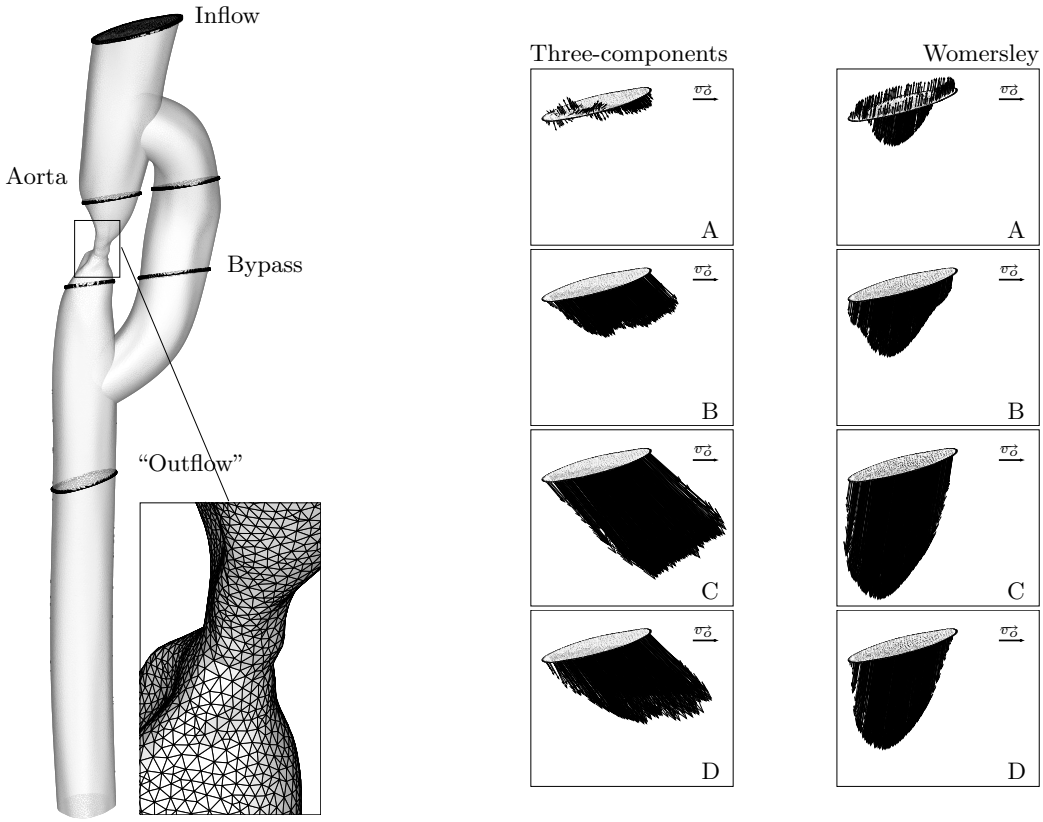

FIGURE 1. Pig anatomy and mesh at the stenosis (left). Cross-sections where flow rate is measured are shown. Measured velocity profiles at the inlet for times A, B, C and D in the cardiac cycle. Corresponding Womersley velocity profiles (right). Reference vector: $\vec{v_o} = 10\ cm.s^{-1}$.

Two different pulsatile velocity profiles are imposed at the inlet of the calculation domain: the actual velocities measured using PC-MRI (including in-plane components,) or an idealized Womersley velocity profile derived from the measured flow rate.

Womersley theory is based on the analytical solution of the Navier-Stokes equations in the case of a fully-developed pulsatile flow in a straight circular cylinder (of radius R). Keeping these assumptions in mind, it can be applied to blood flow: when the flow rate, $\dot{Q}(t)$, is known, the axial velocity profile can be derived. Given the period of the cardiac cycle ($T = 2\pi/\omega$), a Fast Fourier Transform is used to extract the frequency content of the flow waveform.

The Fourier coefficients B_n and the Womersley velocity profile in terms of the radius r and the time t are

$$\dot{Q}(t) = \sum_{n=0}^{N} B_n e^{in\omega t};\ u(r,t) = \frac{2B_o}{\pi R^2}\left[1 - \left(\frac{r}{R}\right)^2\right] + \sum_{n=1}^{N} \frac{B_n}{\pi R^2}\left[\frac{1 - \frac{J_o\left(\alpha_n \frac{r}{R} i^{3/2}\right)}{J_o\left(\alpha_n i^{3/2}\right)}}{1 - \frac{2J_1\left(\alpha_n i^{3/2}\right)}{\alpha_n i^{3/2} J_o\left(\alpha_n i^{3/2}\right)}}\right] e^{in\omega t}$$

where J_o and J_1 are Bessel functions, and $\alpha_n = R\sqrt{(n\omega)/\nu}$.

The Womersley number, α_1, takes the value of 10.8 in our simulations. The period is

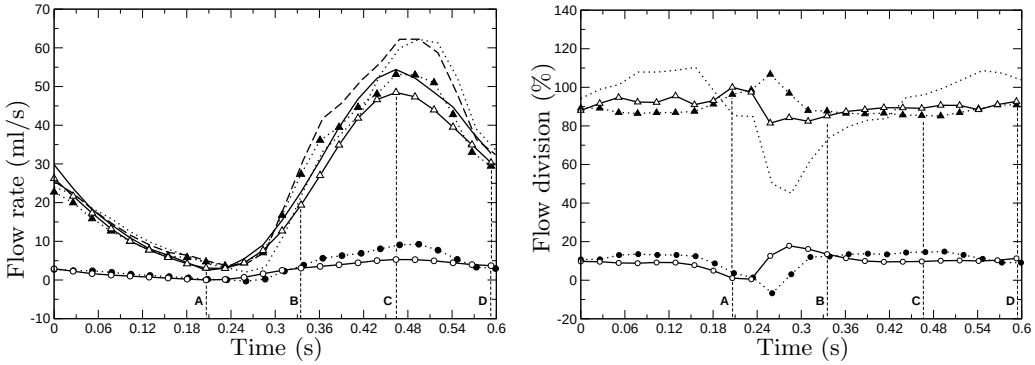

FIGURE 2. Flow rate versus time (left), flow rate ratio versus time (right). ——— : inflow (data), ····· : outflow (data), —○— : aorta (simulation), ··· ●··· : aorta (data), —△— : bypass (simulation), ··· ▲ ··· : bypass (data), — — — : outflow (data aorta + bypass). Time A: end diastole, time B: mid-systole, time C: peak systole, time D: mid-diastole

$T = 0.62$ s. The Reynolds number measured at the inlet varies from 50 at end diastole (time A, figure 2) to 1300 at peak systole (time C, figure 2).

From measured data we calculate the flow rate (figure 2, full line, left). As we do not have a circular inlet, we first calculate the Womersley velocities for a constant radius, R, corresponding to the maximum radius of the lumen. The resulting velocity profile is then mapped on the real geometry. In this model, the measured inflow cross-section is not normal to the vessel path, so that the velocity vectors need to be reoriented. The shape of the velocity profile is kept similar (with zero values at the boundaries and a maximum at the centroid of the vessel), and the flow rate is conserved, leading to a "quasi-Womersley" profile. The measured three-component and idealized velocity profiles are shown on figure 1 (left and right side cross-section respectively) at four representative times in the cardiac cycle (see time A, B, C and D on figure 2). In contrast to the measured three-component velocity profile, which is fairly uniform, the Womersley solution is characterized by a smooth profile. The descending aorta is curved in such a way that the in-plane component of the velocity vectors for the three-component data is not negligible and a large quantity of blood enters the bypass graft.

3. Results

3.1. *Flow rates*

Comparison of the flow division in the simulation and in the experiment show a maximum of 10% discrepancy at peak systole, both in the bypass (figure 2 left, triangles) and in the aorta (figure 2 left, circles). We notice on this graph that the measured flow rate is always larger than the result of the simulation. The flow rate in the simulation was extracted from measurements of the three components of the velocity at the location of the inlet, whereas the data plotted at the location of the aorta and the bypass correspond to through-plane velocity measurements only. The flow rate measured further downstream of the stenosis ("Outflow") with the through-plane technique is also higher than that given by the three-components velocity measurements (figure 2 left, dashed line). Furthermore, the sum of the measured flow rate in the aorta and the bypass (figure 2 left, dotted

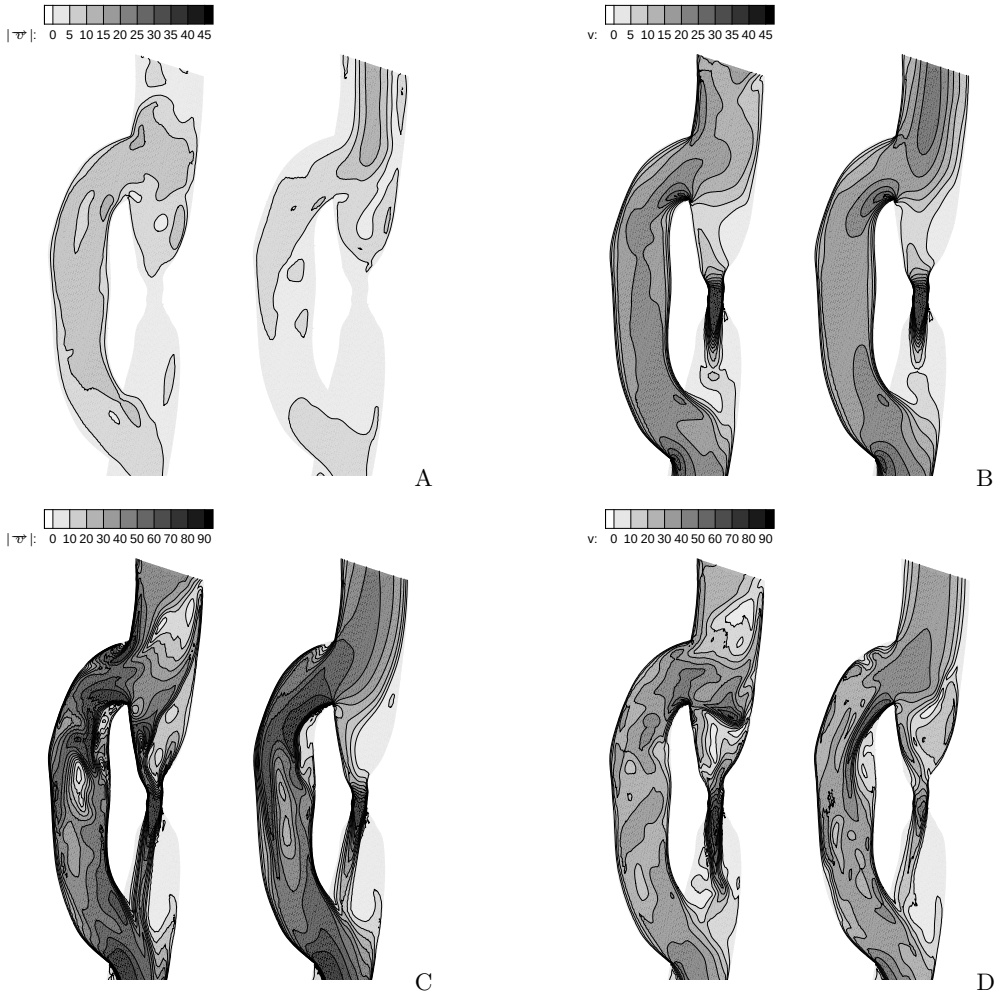

FIGURE 3. Transversal cross-section: comparison of the velocity magnitude (in $cm.s^{-1}$) for the three component case (right) and the Womersley case (left) at times A, B, C, D

line) is not equivalent to that measured (with the same measurement technique) at the outlet (figure 2 left, dashed line). Assuming that the segmentation process of the vessel boundary does not add any error, this difference can be due to a small change in the physiological state of the pig (peak systole is slightly shifted), or illustrates the fact that the vessel wall is compliant.

As the flow division between the two branches is not dependent on which measurement technique was employed, we can still compare simulation and imaging data (figure 2, right). On average, in the simulation, 9.7% of the fluid that enters the domain goes into the aorta (open circles) and 10.5% in the experiment (plain circles). The majority of blood flows into the bypass: 90.3% in the simulation (open triangles) versus 89.5% in the experiments (plain triangles). Due to pulsatile effects, the flow division varies slightly during the cardiac cycle, and particularly at end-diastole, between the deceleration and acceleration phases.

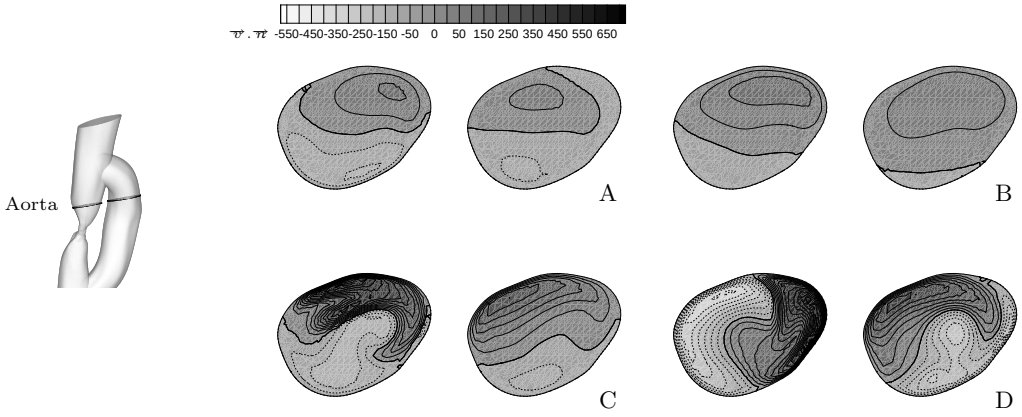

FIGURE 4. Aorta cross-section (above the stenosis): comparison of the through-plane velocity ($\vec{v}.\vec{n}$ in $mm.s^{-1}$) in the three-components case (left) and the Womersley case (right)

Within the generally-accepted 10% error band in MRI measurements, the flow rates in the calculation and the data compare favorably.

3.2. *Influence of inflow profiles: three components and Womersley*

In order to characterize the influence of inflow boundary conditions, we will focus on four representative times in the cardiac cycle (time A, B, C and D, figure 2).

A basic observation that has been previously made in the configuration of a tight stenotic vessel (Khalifa & Giddens 1981) is that a non-periodic behavior from cycle to cycle appears upstream and downstream of the stenosis. Even though the physiological Reynolds numbers at the inflow are small, the reduction in area at the stenosis is large (85%) and pulsatile effects excite vortex shedding. In our model, in addition to the "simple restriction case" studies, the aperiodic stenotic jet is also influenced by the high-velocity fluid coming from the bypass. Both the three-component and the Womersley inlet boundary conditions show this phenomenon. As a consequence, we will focus only on averaged-velocity comparisons between experiment and numerics. We consider the 35 periods following the usual five periods required to initialize the simulation (i.e. about four flow-through times).

The velocity-magnitude field across the domain is plotted in figure 3 for the three-component case (left side of the figure) and for the Womersley case (right side). As expected close to the inflow, one can clearly observe the variations induced by using two different velocity profiles as a boundary condition. At all characteristic times the isocontours of the velocity in the Womersley case are aligned with the vessel centerline at the inlet, whereas the inlet velocity in the three-component case is oriented towards the bypass. This fact locally modifies the fluid mechanics in the domain, but global parameters such as the flow division in the branches are identical in the two cases. The same general features of the flow can be recognized: during systole (acceleration phase, times B and C), a large recirculation zone appears above the stenosis, while high velocities are measured at the stenotic jet. On the inside wall of the bypass graft, the region of separation classically found in curved vessels is observed. Comparing local velocities in the two simulations, we find some variations in the recirculation area above the stenosis, mainly in the deceleration phase (time D, figures 3 and 4). When the flow rate is high, a large vortex is generated above the stenosis (times B and C, figures 3 and 4). In both cases the size of this vortex is similar. During the deceleration phase and later (times D

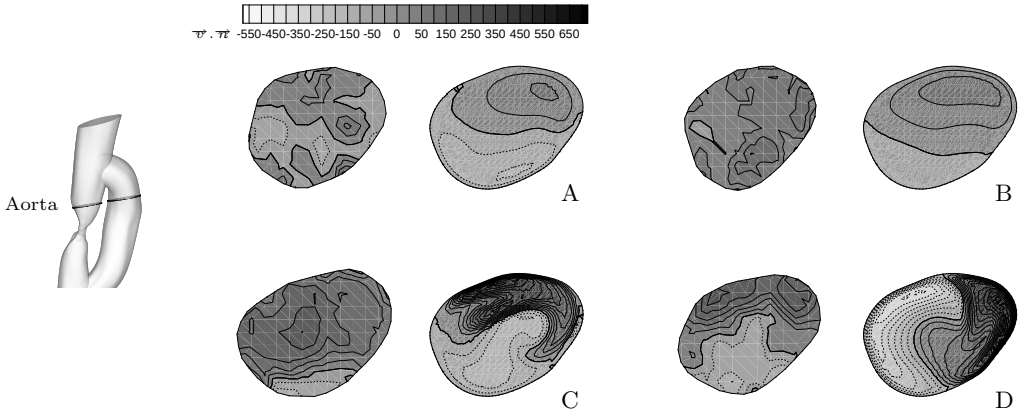

FIGURE 5. Aorta cross-section (above the stenosis): comparison of the through-plane velocity ($\vec{v}.\vec{n}$ in $mm.s^{-1}$) in experiments (left) and the simulation in the three-components case (right).

and A, 3), the flow is more perturbed and vortex shedding occurs, leading to different behavior in the two cases. In the bypass graft, at all times in the cardiac cycle, the extent of the separation region is more pronounced in the Womersley case. On figure 3, the jet is also influenced by the boundary conditions downstream of the stenosis.

Using physiological boundary conditions has an impact on local velocity. Whether these variations of the flow field are large enough to cause, or modify the development of, thrombosis is still an open question.

3.3. *Comparison of experiment and simulation*

Figure 5 shows the through-plane velocity obtained in the simulation (in the "realistic" three-component case) and in the experiments at an aortic cross-section above the stenosis. The velocities are similar, which is consistent with what we observed above: the flow rates in the experiments and in the calculations compare well. When comparing local velocity patterns, the results do not agree. The maxima of the velocity are shifted between the data and the simulation (time D, figure 5).

The comparison is not conclusive. On the experimental data, the isocontours of the velocity are noisy, particularly at end-diastole and during the acceleration phase (times A and B, figure 5). At peak systole and mid-diastole (times C and D, figure 5), the velocity profiles corresponding to the experiments look erratic and do not reflect the complexity of the contours found in the simulation.

Steinman (2002) reports in a review that MRI is likely to fail when measuring sudden local changes in the flow field and in the presence of complex flow patterns. To add to the difficulty of measuring accurate velocity fields *in vivo* (the pig has to be kept in the same physiological state), the possible sources of error in the procedure involved in the simulation are numerous. The volumetric images (MRA), as well as the two-dimensional MRI data, need to be segmented in order to build the geometric model and to extract the velocity vectors at a specific location. Even using an automatic segmentation program to avoid human subjectivity, an error of a few pixels may induce some variations in the calculation and in comparing the velocity profiles.

4. Conclusion and future plans

From measurements of the velocity vectors in the aortic vessel, above the restriction, we observe that its characteristics differ from the analytical solution of a pulsatile flow. We have demonstrated numerically that the flow field in the domain is modified when using one inflow condition or the other. We believe that using the "true" velocity profile as a boundary condition in the simulation is essential when trying to understand the evolution of diseases. In one of the experiments, a clot formed in the separation region in the bypass, a typical region of the flow where we obtained differences in the velocity between the two cases. While the measured division of the flow rate between the two passages is well predicted in the simulation, detailed flow patterns do not seem to be captured properly by the measurements. More complex *in vitro* experiments, with large flow variations, should be considered for validation purposes. Further, the influence of variations in geometry should be evaluated.

REFERENCES

Botnar, R., Rappitsch, G., Scheidegger, M. B., Liepsch, D., Perktold, K. & Boesiger, P. 2000 Hemodynamics in the carotid artery bifurcation: A comparison between numerical simulation and *in vitro* MRI measurements. *J. Biomech.* **33**, 137–144.

Cebral, J. R. & Lohner, R. 2001 From medical images to anatomically accurate finite element grids. *Int. J. Num. Methods Engng.* **21**, 985–1008.

Dilley, R. J., Mc Geachie, J. K. & Prendergast, F. J. 1988 A review of the histologic-changes in vein-to-artery grafts with particular reference to intimal hyperplasia. *Arch. Surg.* **123**, 691–696.

Gewertz, B. L., Graham, A., Lawrence, P. F., Provan, J. & Zarins, C. K. 1992 Diseases of the vascular system. *Essentials of general surgery*, Lippincott Williams & Wilkins, Philadelphia, pp. 328–347.

Jansen, K. E., Whiting, C. H. & Hulbert, G. M. 2000 A generalized-alpha method for integrating the filtered Navier-Stokes equations with a stabilized finite element method. *Comput. Meth. Appl. Mech. Engrg.* **190**, 305–319.

Khalifa, A. M. A. & Giddens, D. P. 1981 Characterization and evolution of post-stenotic flow disturbances. *J. Biomech.* **14**, 279–296.

Ku, J. P., Draney, M. T., Arko, F. R., Lee. W. A., Chan, F., Pelc, N. J., Zarins, C. K. & Taylor, C. A. 2002 *In Vivo* validation of numerical predictions of blood flow in arterial bypass grafts. *Ann. of Biomed. Engng.* **30**, 743–752.

Milner, J. S., Moore, J. A., Rutt, B. K., & Steinman, D. A. 1998 Hemodynamics of human carotid artery bifurcations: Computational studies with models reconstructed from magnetic resonance imaging of normal subjects. *J. Vasc. Surg.* **28**, 143–156.

Perktold, K. & Rappitsch, G. 1995 Computer-simulation of local blood-flow and vessel mechanics in a compliant carotid-artery bifurcation model. *J. Biomech.* **28**, 845–856.

Perktold, K., Resch, M. & Peter, R. 1991 Three-dimensional numerical analysis of pulsatile flow and wall shear stress in the carotid artery bifurcation. *J. Biomech.* **24**, 409–420.

Steinman, D. A. 2002 Imaged-based computational fluid dynamics modeling in realistic arterial geometries *Ann. Biomed. Engrg.* **30**, 483–497.

Taylor, C. A., Draney, M. T, Ku, J. P., Parker, D., Steele, B. N., Wang, K. & Zarins, C. K. 1999 Predictive medicine: Computational techniques in therapeutic decision-making. *Computer Aided Surgery* **4**, 231–247.

Taylor, C. A., Hugues, T. J. R. & Zarins, C. K. 1996 Computational investigations in vascular disease. *Computers in Physics* **10**, 224–232.

Taylor, C. A., Hugues, T. J. R. & Zarins, C. K. 1998 Finite element modeling of flow in arteries. *Comput. Methods Appl. Mech. Engrg.* **158**, 155–196.

Taylor, C. A., Hugues, T. J. R. & Zarins, C. K. 1998 Finite element modeling of 3-dimensional pulsatile flow in the abdominal aorta: relevance to atherosclerosis. *Ann. Biomed. Engrg.* **26**, 1–13.

Taylor, C. A., Hugues, T. J. R. & Zarins, C. K. 1999 Effect of exercise on hemodynamic conditions in the abdominal aorta. *J. Vasc. Surg.* **29**, 1077–89.

Zarins, C. K. & Taylor, C. A. 1998 Hemodynamic Factors in Atherosclerosis *Vascular surgery: a comprehensive review* (W. S. Moore, ed.) Saunders Company/Elsevier, Amsterdam, pp. 97-110.

Wang, K. C, Dutton, R. W. & Taylor, C. A. 1999 Level Sets for vascular model construction in computational hemodynamics *IEEE Engineering in Medicine and Biology.* **18**, 33–39.